

















CrossMark

# Kinetic-scale Spectral Features of Cross Helicity and Residual Energy in the Inner Heliosphere

Daniel Vech<sup>1,2</sup> , Justin C. Kasper<sup>1,3</sup> , Kristopher G. Klein<sup>4</sup> , Jia Huang<sup>1</sup> , Michael L. Stevens<sup>3</sup> , Christopher H. K. Chen<sup>5</sup> , Anthony W. Case<sup>3</sup> , Kelly Korreck<sup>3</sup> , Stuart D. Bale<sup>6</sup> , Trevor A. Bowen<sup>6</sup> , Phyllis L. Whittlesey<sup>6</sup>, Roberto Livi<sup>6</sup>, Davin E. Larson<sup>6</sup>, David Malaspina<sup>2</sup> , Marc Pulupa<sup>6</sup> , John Bonnell<sup>6</sup>, Peter Harvey<sup>6</sup>, Keith Goetz<sup>7</sup>, Thierry Dudok de Wit<sup>8</sup> , and Robert MacDowall<sup>9</sup> 

<sup>1</sup>Climate and Space Sciences and Engineering, University of Michigan, Ann Arbor, MI, USA

<sup>2</sup>Laboratory for Atmospheric and Space Physics, University of Colorado, Boulder, CO, USA

<sup>3</sup>Smithsonian Astrophysical Observatory, Cambridge, MA, USA

<sup>4</sup>Lunar and Planetary Laboratory, University of Arizona, Tucson, AZ, USA

<sup>5</sup>School of Physics and Astronomy, Queen Mary University of London, London E1 4NS, UK

<sup>6</sup>Space Science Laboratory, University of California Berkeley, Berkeley, CA, USA

<sup>7</sup>School of Physics and Astronomy, University of Minnesota, Minneapolis, MN, USA

<sup>8</sup>LPC2E, CNRS and University of Orléans, Orléans, France

<sup>9</sup>NASA Goddard Space Flight Center, Greenbelt, MD, USA

Received 2019 September 10; revised 2019 November 21; accepted 2019 December 9; published 2020 February 3

## Abstract

In this work, we present the first results from the flux angle (FA) operation mode of the Faraday Cup instrument on board the *Parker Solar Probe* (*PSP*). The FA mode allows rapid measurements of phase space density fluctuations close to the peak of the proton velocity distribution function with a cadence of 293 Hz. This approach provides an invaluable tool for understanding kinetic-scale turbulence in the solar wind and solar corona. We describe a technique to convert the phase space density fluctuations into vector velocity components and compute several turbulence parameters, such as spectral index, residual energy, and cross helicity during two intervals when the FA mode was used in *PSP*'s first encounter at 0.174 au distance from the Sun.

*Unified Astronomy Thesaurus concepts:* [Heliosphere \(711\)](#); [Interplanetary turbulence \(830\)](#); [Solar wind \(1534\)](#); [Magnetohydrodynamics \(1964\)](#); [Alfvén waves \(23\)](#)

## 1. Introduction

The solar wind is a hot, tenuous plasma propagating away from the Sun's surface, which is ubiquitously observed in a turbulent state (Coleman 1968). Turbulence in the solar wind is modeled as a cascade of energy from the outer scales to the much smaller dissipative scales through an inertial range. In the inertial range, the velocity and magnetic fluctuations are largely perpendicular to the local magnetic field direction and the spectral index of the power spectra of the magnetic and velocity fluctuations are close to  $-5/3$  and  $-3/2$ , respectively (Coleman 1968; Matthaeus & Goldstein 1982; Podesta et al. 2007; Boldyrev et al. 2011). Below this range, roughly coincident with the convected ion-kinetic scales, the magnetic energy spectrum steepens and Alfvénic turbulence undergoes a transition into dispersive kinetic Alfvén waves (Bale et al. 2005; Chen et al. 2013b). Between ion and electron scales, the spectral index of the magnetic fluctuations is typically between  $-2$  and  $-4$  (Leamon et al. 1998; Smith et al. 2006; Alexandrova et al. 2009; Matteini et al. 2016).

In contrast to magnetic fields, the power spectrum of velocity fluctuations in the kinetic range is much less understood largely due to the fact that high-cadence plasma moment measurements in the solar wind only recently became available. Studies based on Spektr-R data (proton moments with 31 ms cadence measured by six Faraday Cups) presented the first results on the

high-frequency part (up to 2 Hz) of the velocity power spectrum, including the break frequency and spectral indices (Šafránková et al. 2013a, 2013b, 2016; Riazantseva et al. 2017). Unfortunately, the lack of an operating magnetic field instrument of Spektr-R made it impossible to study correlation between high-frequency velocity and magnetic fluctuations and to compute cross helicities and residual energies.

Cross helicity is defined as  $\sigma_c = (E^+ - E^-)/(E^+ + E^-)$  where  $E^\pm$  corresponds to the power spectra of the Elsässer variables  $z^\pm = \delta v \pm \delta b / \sqrt{\mu_0 \rho}$  where  $\delta v$  and  $\delta b$  are the fluctuations of the velocity and magnetic fields in Alfvén units, respectively, and  $\rho$  is the mean mass density of protons (Chen et al. 2013a; Wicks et al. 2013). Cross helicity is normalized in such a way that it is 1 and  $-1$  for anti-sunward and sunward propagating waves, respectively. Cross helicity is conserved in the absence of dissipation and corresponds to the linkages between lines of vorticity and magnetic field lines, both of which are frozen to the fluid flow in the absence of dissipation (Chandran 2008). In addition to the numerous statistical studies at 1 au (e.g., Chen et al. 2013a; Wicks et al. 2013), the radial dependence of  $\sigma_c$  was investigated on magnetohydrodynamic (MHD) scales with *Helios* data (Roberts et al. 1987; Grappin et al. 1990; Bruno & Bavassano 1991, 1993; Bruno et al. 1997). These studies found that  $\sigma_c$  decreases as the solar wind propagates away from the Sun; however, the physical mechanisms responsible for this feature are debated. For example, Bruno & Bavassano (1991, 1993) suggested that the decrease of  $\sigma_c$  is driven by the interaction of Alfvénic fluctuations with static structures or magnetosonic perturbations, which results in a decrease of the  $z^+$  component rather than an increase of  $z^-$ . Several other



Original content from this work may be used under the terms of the [Creative Commons Attribution 4.0 licence](#). Any further distribution of this work must maintain attribution to the author(s) and the title of the work, journal citation and DOI.

studies suggested that shear and expansion causes the decrease of  $\sigma_c$  with increasing radial distances (e.g., Roberts et al. 1987; Oughton & Matthaeus 1995).

Residual energy is the difference between the kinetic and magnetic energy and is defined as  $\sigma_r = (E^v - E^b)/(E^v + E^b)$ . Unlike for pure Alfvén waves (Alfvén 1942) where the energy of velocity and magnetic fluctuations are in equipartition, in the solar wind, the magnetic energy is typically larger than the energy of velocity fluctuations (Chen et al. 2013a; Wicks et al. 2013). The origin of this difference is a matter of considerable debate; potential explanations include the role of magnetic structures with the solar origin and local generation of residual energy by counterpropagating Alfvén wave packets (Wang et al. 2011; Boldyrev et al. 2012; Bowen et al. 2018).

Understanding the scaling of  $\sigma_r$  and  $\sigma_c$  in the kinetic-scale solar wind fluctuations is fundamentally important for describing heating and dissipation in the solar wind, solar corona, and plasma systems more generally. Previous turbulence models (e.g., Boldyrev 2006; Matthaeus et al. 2008) described the coupling between velocity and magnetic field fluctuations in the inertial range; however, the main assumptions underlying these models are violated at the kinetic scales where the MHD approximation breaks down and the quadratic integral invariants are no longer retained (Matthaeus & Goldstein 1982). To the best of our knowledge, no theory exists that describes the correlation between velocity and magnetic fluctuations in the kinetic range. The first attempt to measure  $\sigma_c$  and  $\sigma_r$  in the kinetic range was presented by Parashar et al. (2018) using *Magnetospheric Multiscale Mission* data. They found that  $\sigma_r$  and  $\sigma_c$  converge to 1 and 0, respectively, from the inertial range to the smallest observable scales (20–40 km). The loss of alignment between  $\delta\mathbf{v}$  and  $\delta\mathbf{b}$  (quantified by the metric  $\cos(\theta) = \sigma_c/\sqrt{(1 - \sigma_r^2)} \approx 0$ ) was explained by the demagnetization of protons.

The Faraday Cup (SPC) instrument (Kasper et al. 2016; Case et al. 2020) on board NASA’s *Parker Solar Probe* (*PSP*; Fox et al. 2016) is equipped with a novel flux angle (FA) operation mode that allows rapid measurements of the phase space density fluctuations with an unprecedented 293 Hz cadence, providing a new tool to understand kinetic-scale turbulence in the solar wind and solar corona. SPC was operated in FA mode twice for a total of  $\sim 110$  s during the first perihelion of the *PSP* on 2018 November 4 and captured the fine structure of a magnetic switchback. Magnetic switchbacks are one of the most prominent features of the solar wind in the inner heliosphere; they are characterized by short, large-amplitude velocity enhancements that are accompanied with a  $90^\circ$ – $180^\circ$  rotation of the magnetic field (Gosling et al. 2011; Horbury et al. 2018; Dudok de Wit et al. 2020). These structures might be direct signatures of impulsive chromospheric or coronal energy release (Horbury et al. 2018; Bale et al. 2019).

In this work, we present the first results from the FA operation mode of SPC and study  $\sigma_c$  and  $\sigma_r$  in the kinetic range of the turbulent cascade. Our study complements the ones by McManus et al. (2020), Chen et al. (2020), and Parashar et al. (2020), which focus on magnetic and velocity fluctuations on MHD scales in the inner heliosphere. In Section 2, we describe the conversion of phase space fluctuations into vector velocity fluctuations, with particular emphasis on the underlying assumptions and limitations of the data product. In Section 3, we discuss the properties of kinetic-scale turbulence in the observed magnetic switchback, such as a spectral index of the

power spectrum, residual energy, and cross helicity. Finally, Section 4 contains a summary and a discussion of the results.

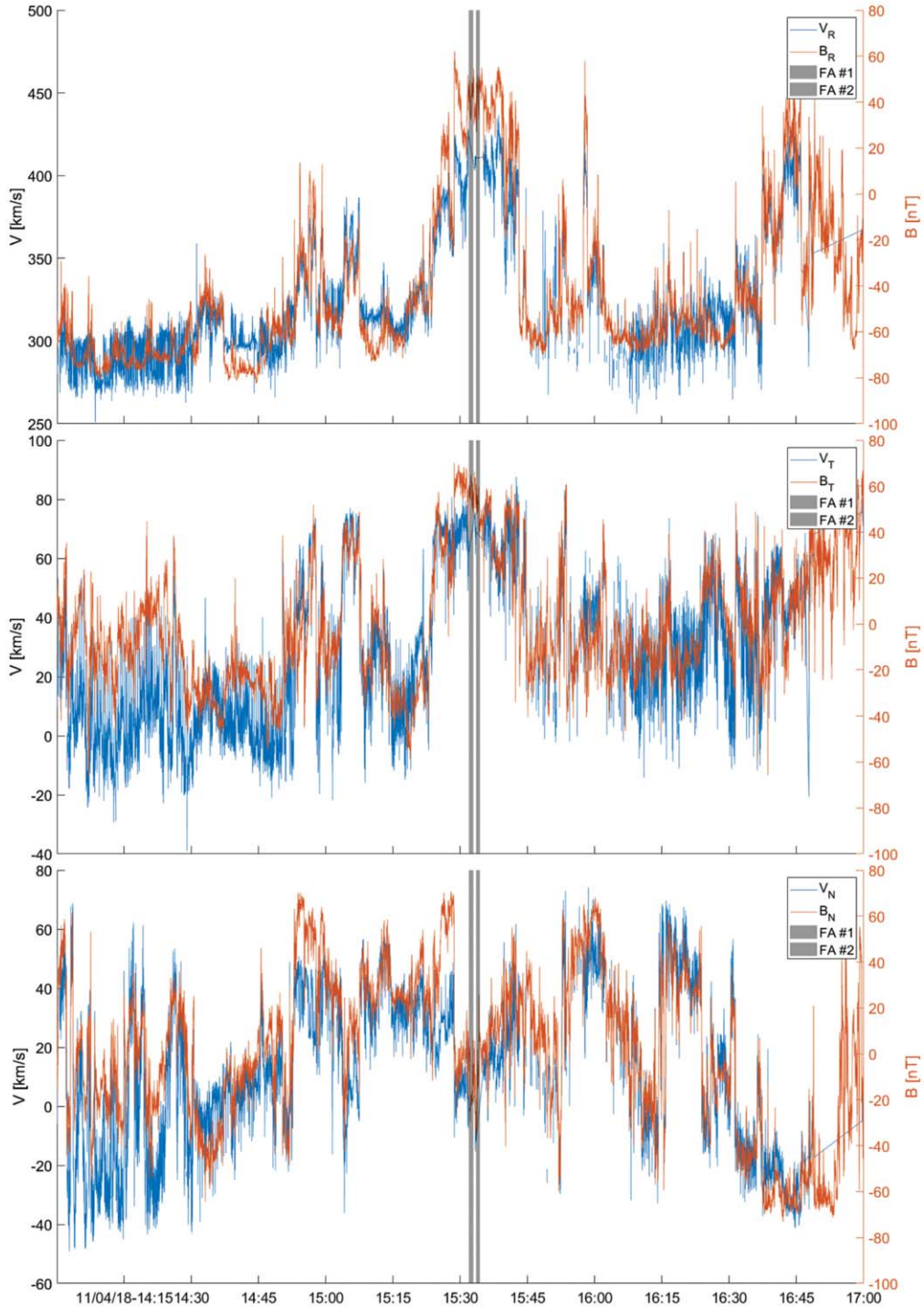
## 2. Method

The Faraday Cup instrument of the *PSP* measures fluxes and flow angles as a function of energy from 50 eV/q to 8 keV/q for ions (Kasper et al. 2016; Case et al. 2020) based on the currents detected by four collector plates. In typical operation mode, SPC scans through 128 energy per charge windows in 0.87 s (1.14 Hz); higher-cadence data products ( $\sim 5$ – $19.6$  Hz) are available for shorter intervals as well. In FA mode SPC measures a single energy/charge window near the center of the proton velocity distribution function (VDF) with 293 Hz cadence.

Figure 1 shows an overview of the components of the magnetic field (293 Hz cadence based on fluxgate magnetometer data; Bale et al. 2016) and velocity for a 3 hr period starting on 2018 November 4 14:00:00 UT when the *PSP* was approximately at 0.174 au distance from the Sun. The vector components are in the Radial Tangential Normal (RTN) coordinate system where  $R$  points radially outward from the Sun,  $N$  is along the ecliptic north, and  $T$  completes the right-hand coordinate system. A magnetic switchback was observed from 15:24:01 to 15:43:07 and was accompanied with a sudden reversal of the radial magnetic field component and enhanced (toward the positive  $T$  direction) tangential velocity component. The duration of the studied magnetic switchback (e.g., interval with  $B_R > 0$  nT) is approximately 19 minutes, which is considered to be an above average structure (see Kasper et al. 2019). In Figure 1, the shaded region marks the two intervals where SPC was operated in FA mode between 15:31:54–15:32:53 and 15:33:30–15:34:22 UT.

Figure 2 shows 15 s averages of proton VDFs before each FA mode interval where the  $x$ -axis is the phase speed and the  $y$ -axis is the phase space density ( $P$ ) in arbitrary units (for the conversion of the axes, see Case et al. 2020). The FA mode achieves unprecedented temporal resolution by scanning a single window in phase space near the peak of the VDF, which are marked with blue ( $446$ – $457$  km s $^{-1}$ ) and red ( $426$ – $437$  km s $^{-1}$ ) for the first and second FA mode intervals, respectively. Significant changes in the solar wind parameters shift the VDF, hence the blue and red regions do not align with the peak, which makes the interpretation of the FA mode measurements more complicated. To ensure that the FA mode interval is not affected by those large changes, we studied the variability of the solar wind parameters and compared 15 s averages of the solar wind speed ( $V_{sw}$ ), the core proton density ( $n_p$ ), the core thermal velocity ( $V_{th}$ ), the ratio of thermal to magnetic pressure ( $\beta_p$ ), and Alfvén speed ( $V_A$ ), which are summarized in Table 1. The solar wind parameters were very steady during the studied periods and none of them show variations of more than 5% suggesting that SPC measured approximately the same part of the VDF throughout in the FA mode intervals. We note that the proton core temperature anisotropy ( $T_\perp/T_\parallel$  estimated with 10 s cadence; for details, see Huang et al. 2019) was in the range of 0.96–1.07 for both intervals.

The goal of the subsequent analysis is to define a fitting procedure converting the FA mode data into vector velocity components and to estimate the potential noise contribution from  $n_p$  and  $V_{th}$  fluctuations. Our approach is the following: full proton VDFs from 15:30:54 to 15:35:22 UT (starting 60 s



**Figure 1.** Overview of the magnetic and velocity components in a 3 hr interval centered at the FA mode data.

before the first and ending 60 s after the second FA mode interval) were selected where plasma moments (including  $V_{sw}$ ,  $n_p$  and  $V_{th}$ ) were available. Three linear fits were used to estimate the scaling of  $P$  with  $V_{sw}$ ,  $n_p$  and  $V_{th}$ . For the fitting, the phase space densities in the 445–457 and 426–437  $\text{km s}^{-1}$  windows were normalized by their mean values based on the entire interval ( $\tilde{P} = P/\langle P \rangle$ ). The slopes ( $L_{1,2}$ ) and intercepts ( $M_{1,2}$ ) of the fits are summarized in Table 2. We note that in the studied interval  $P$  varies over a relatively small range, and thus higher order fits lead to no meaningful improvement in the goodness of these fits.

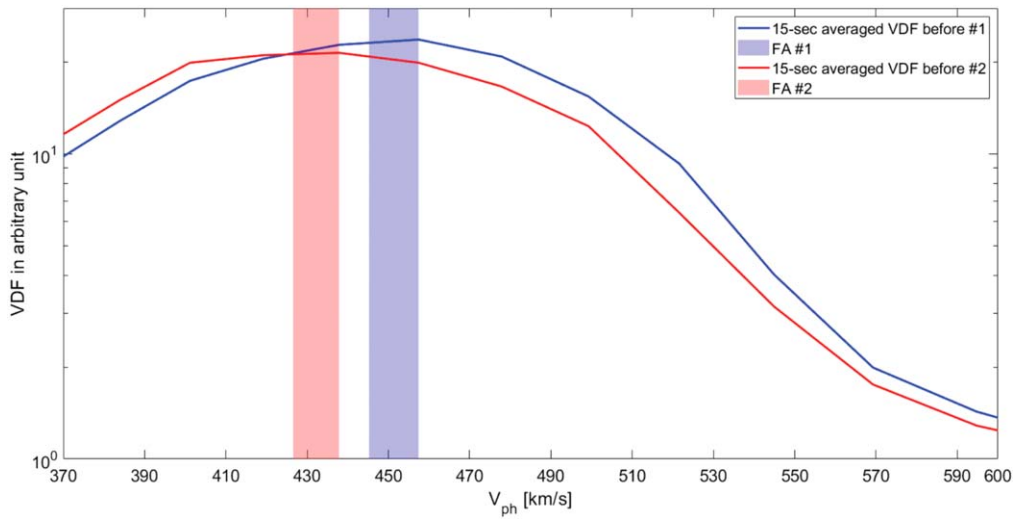
The vector velocity components in the RTN frame were obtained as

$$V_R = [\cos(\phi) \cdot \cos(\theta) \cdot ((L_{V_{sw1,2}} \cdot \tilde{P}_{1,2}) + M_{V_{sw1,2}})] - V_{R_{S/C}} \quad (1)$$

$$V_T = [\cos(\phi) \cdot \sin(\theta) \cdot ((L_{V_{sw1,2}} \cdot \tilde{P}_{1,2}) + M_{V_{sw1,2}})] - V_{T_{S/C}} \quad (2)$$

$$V_N = [\sin(\phi) \cdot ((L_{V_{sw1,2}} \cdot \tilde{P}_{1,2}) + M_{V_{sw1,2}})] - V_{N_{S/C}} \quad (3)$$

$$\phi = \frac{2\pi}{180} \lambda \left[ \frac{(C + D) - (A + B)}{A + B + C + D} \right] \quad (4)$$



**Figure 2.** 15 s averages of full VDFs before each FA mode interval, respectively. The shaded areas mark the range in phase speed, which are measured in the FA mode.

**Table 1**  
15 s Averages and Standard Deviations of Solar Wind Parameters before and after Each FA Mode Interval

Parameter	Before #1	After #1	Before #2	After #2
$V_{sw}$ (km s <sup>-1</sup> )	423.5 ± 5.3	415.9 ± 12.1	406.7 ± 4.1	421 ± 4.2
$n_p$ (cm <sup>-3</sup> )	231.5 ± 16.9	230.1 ± 19.4	241.3 ± 9.8	231.7 ± 16.7
$V_{th}$ (km s <sup>-1</sup> )	78.0 ± 5.7	82.7 ± 5.9	85.9 ± 3.4	81.7 ± 5.7
$\beta_p$	0.6 ± 0.17	0.63 ± 0.16	0.71 ± 0.08	0.77 ± 0.2
$V_A$ (km s <sup>-1</sup> )	102.1 ± 5.1	104.7 ± 4.6	102.3 ± 2.2	96.9 ± 3.5

**Table 2**  
Fitting Parameters for the 445–457 km s<sup>-1</sup> ( $L_1$  and  $M_1$ ) and 426–437 km s<sup>-1</sup> ( $L_2$  and  $M_2$ ) Phase Space Density Fluctuations, Respectively

Response Variable	$L_1$	$L_2$	$M_1$	$M_2$
$V_{sw}$	111.19	87.677	320.16	337.67
$V_{th}$	-43.973	-48.672	126.76	131.46
$n_p$	-76.941	-46.356	311.69	281.1

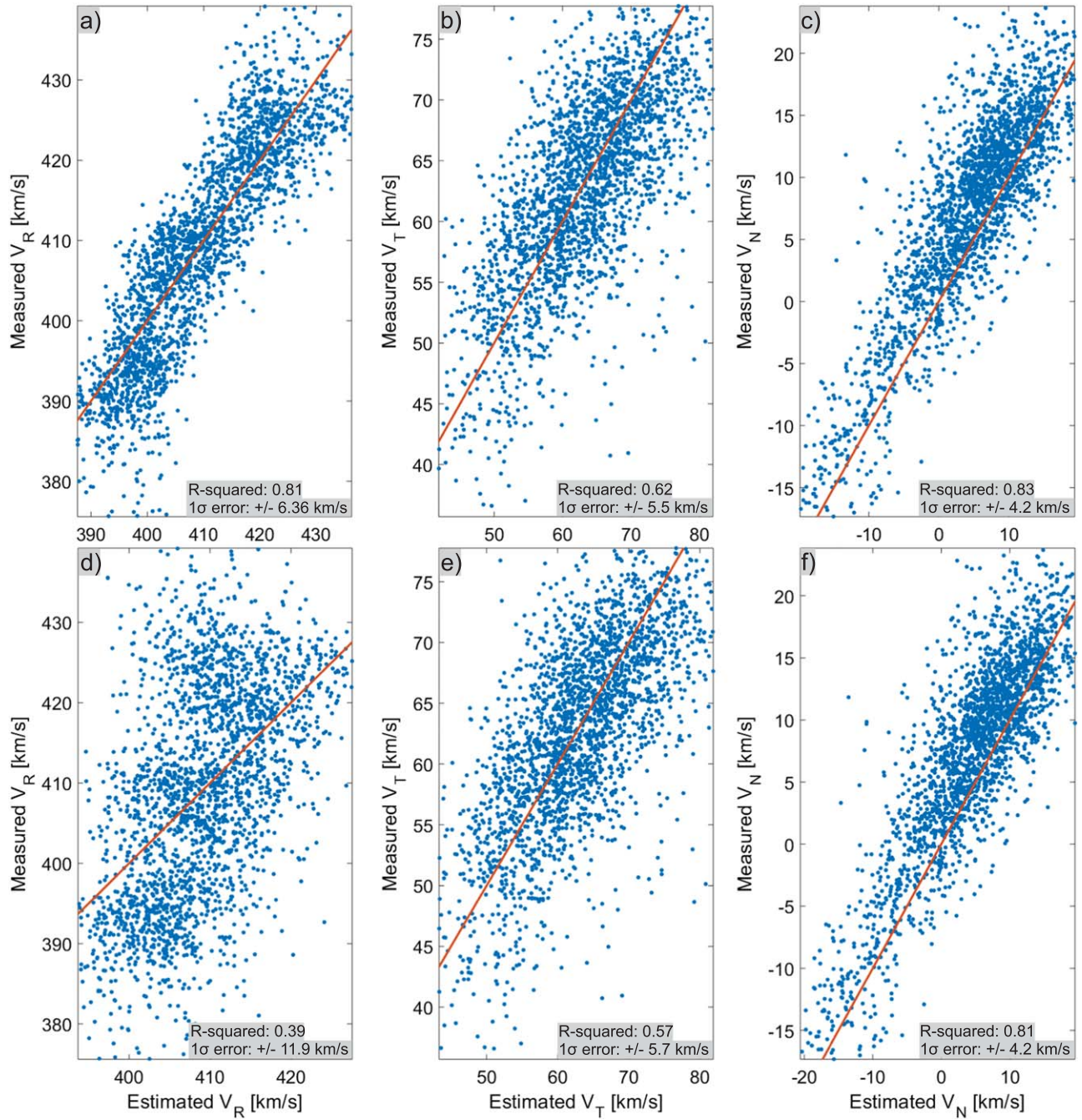
$$\theta = \frac{2\pi}{180} \lambda \left[ \frac{(A + D) - (B + C)}{A + B + C + D} \right]. \quad (5)$$

Equations (4) and (5) are linear approximations of the flow angles where the constant  $\lambda = (\pi/2) * (r_{LA}/d_{LA}) \approx 1.009$  is determined by the radius of the limiting aperture,  $r_{LA} = 10.86$  mm, and its axial distance from the collector plates,  $d_{LA} = 16.9$  mm. The denominator of Equations (4) and (5) corresponds to the sum of currents measured by the four collector plates ( $A$ ,  $B$ ,  $C$ , and  $D$ ) of SPC. As viewed from the Sun during encounter,  $A$  and  $B$  collector plates are on the “ecliptic south,” while  $C$  and  $D$  are on the “ecliptic north.” Equation (4) thus measures the elevation angle of the flow from the  $R$ - $T$  plane toward the  $N$ + direction. Similarly, the numerator of Equation (5) corresponds to currents in the “east–west” direction and thus  $\theta$  is the azimuth angle of the flow, which is measured in the  $R$ - $T$  plane from the  $R$ + direction toward  $T$ + direction (for details of the operation of SPC see Case et al. 2020). In Equations (1)–(3),  $\tilde{P}_{1,2}$  is the normalized phase space density in the 445–457 and

426–437 km s<sup>-1</sup> windows,  $V_{isc}$  is the  $i$ th component of the spacecraft velocity in the RTN frame ( $V_{Rsc} = 18.17$  km s<sup>-1</sup>,  $V_{Tsc} = -90.7$  km s<sup>-1</sup>, and  $V_{Nsc} = -4.1$  km s<sup>-1</sup> during both intervals).

Figure 3 compares the directly measured (based on 19.6 Hz moments) and estimated (using Equations (1)–(5)) RTN velocity components for the 445–457 km s<sup>-1</sup> (a)–(c) and 426–437 km s<sup>-1</sup> (d)–(f) phase space density fluctuations, respectively. The corresponding  $R$ -squared values and  $1\sigma$  errors are shown in each panel; the red line is  $x = y$ . Figure 4 has the same format as Figure 3 and shows the measured and estimated  $n_p$  and  $V_{th}$  values. For the 445–457 km s<sup>-1</sup> phase speed (Figures 4(a)–(c)), the predicted RTN velocity components are in excellent agreement with the high-cadence moments. Figures 4(a)–(b) shows that the predictive power of  $P$  is somewhat lower for  $V_{th}$  and  $n_p$ , resulting in lower  $R$ -squared values. For the lower phase speed range (Figures 4(d)–(f)), we found some scattering in the  $V_R$  component, while the  $T$  and  $N$  velocity components are in good agreement with the measured values. In Figures 4(c)–(d),  $V_{th}$  and  $n_p$  are predicted with larger errors than in Figures 4(a)–(b) and the fits have the lowest  $R$ -squared.

We use our fitting technique to estimate the vector velocity fluctuations in the FA mode and compare their spectral properties to the velocity moments derived based on full VDFs. We selected 190 s of data between 15:28:44–15:31:54 and 15:34:33–15:37:32 (e.g., measurements right before and after the first and second FA mode intervals, respectively) when SPC measured full VDFs with 19.6 Hz cadence. The length of this interval was chosen such that it is long enough to

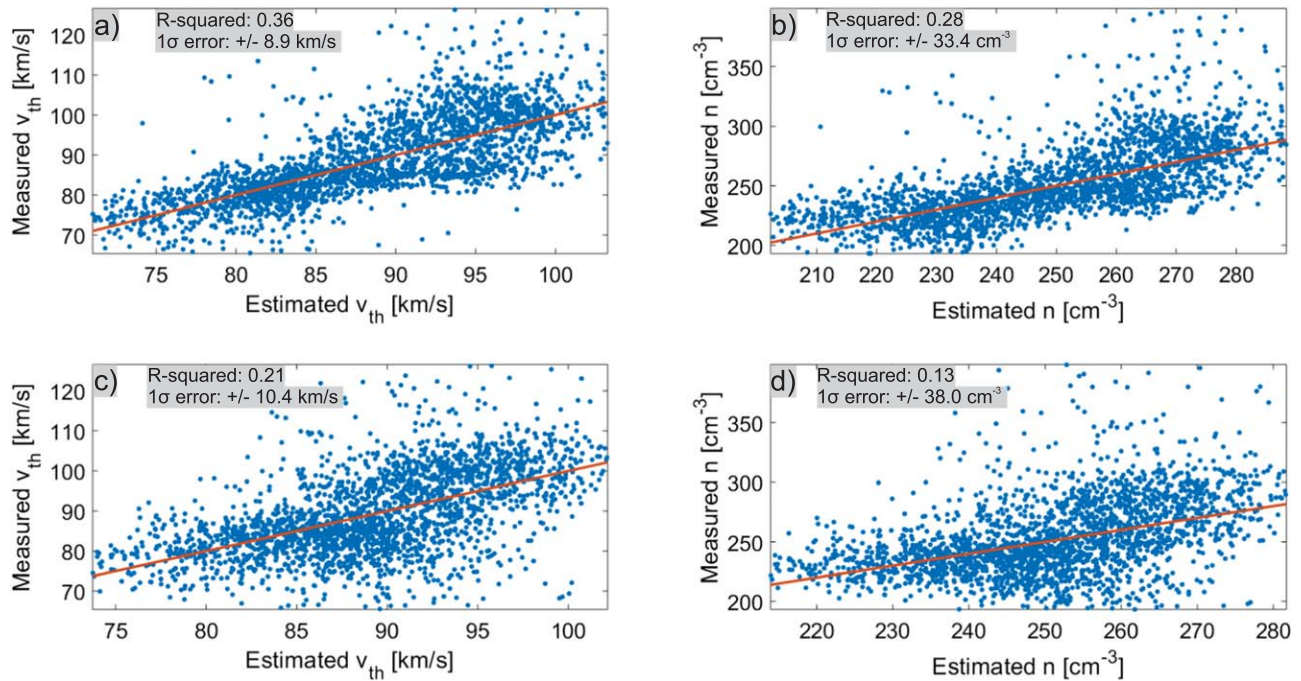


**Figure 3.** Comparison of the measured (based on 19.6 Hz moments) and estimated (Equations (1)–(5)) RTN velocity components for the 445–457  $\text{km s}^{-1}$  (a)–(c) and 426–437  $\text{km s}^{-1}$  (d)–(f) phase space density fluctuations, respectively.

cover the inertial range of the fluctuations, but also all data points are within the magnetic switchback. The trace power spectrum of the velocity fluctuations was computed for the 19.6 Hz data in the magnetic switchback and compared to the spectrum of fluctuations derived from the FA mode data. The results in Figure 5 suggest that the two data sets have remarkably good agreement for low frequencies (below 1 Hz) for both the first (a) and second (b) FA mode intervals. We note that in the case of the 19.6 Hz data switching between neighboring energy/charge windows during the scans may

introduce some noise, which results in a higher noise floor compared to the FA mode data.

Figure 4 indicates that the  $P$  fluctuations are correlated with  $V_{th}$  and  $n_p$  as well, which may introduce noise in the velocity power spectra in Figure 5. To quantify this effect, we used the first FA mode interval and calculated the RTN velocity components,  $V_{th}$  and  $n_p$ . Each parameter was normalized to its median value (e.g., each velocity component separately) and then the power spectra were computed. In Figure 6, it can be seen that the wave power of the trace velocity fluctuations is



**Figure 4.** Comparison of the measured (based on 19.6 Hz moments) and estimated  $n_p$  and  $V_{th}$  for the 445–457  $\text{km s}^{-1}$  (a)–(b) and 426–437  $\text{km s}^{-1}$  (c)–(d) phase space density fluctuations, respectively.

three orders of magnitude larger than the wave power of  $n_p$  and  $V_{th}$ . This significant difference is explained by the fact that the flow angle shows rapid and large-amplitude fluctuations (as expected for a highly Alfvénic flow), while  $n_p$  and  $V_{th}$  change much more slowly. Based on these results, we suggest that the velocity spectra has negligible noise contribution from changes in  $n_p$  and  $V_{th}$ .

### 3. Spectral Features of Kinetic-scale Turbulence

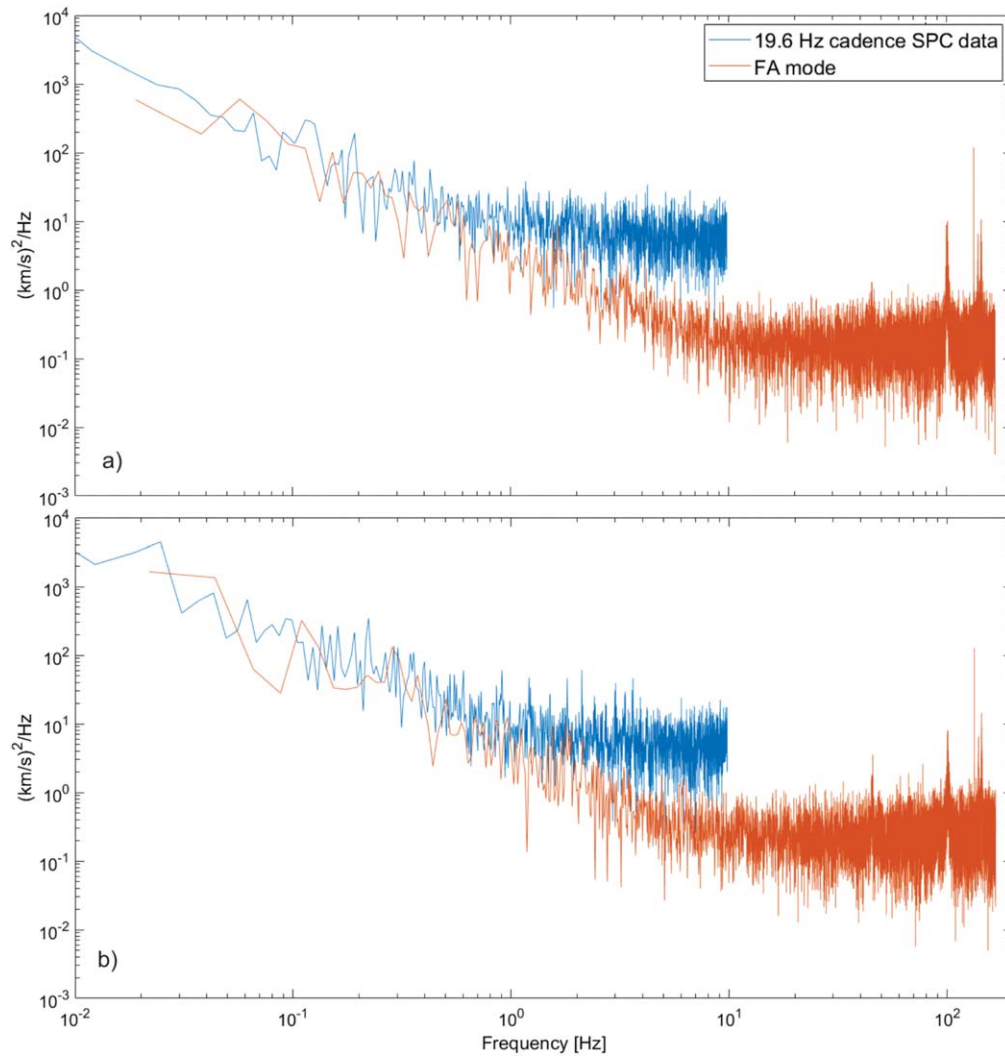
Figures 7(a) and (b) show the power spectrum of the trace velocity and magnetic fluctuations. The magnetic field fluctuations were converted into Alfvén units normalizing by  $(\mu_0 \rho)^{1/2}$ . The vertical lines mark the scale of the convected ion inertial length ( $V_{sw}/2\pi d_i$ ) and proton gyroradius ( $V_{sw}/2\pi \rho_i$ ) where  $d_i = c/\omega_p$  and  $\rho_i = mv_{\perp}/qB$ . The black and green dots show the  $V$ - and  $B$ -field spectral indices based on a fitting window, which has a size of a factor of 3.7; the dots are placed at the center of each fitting window.

In the inertial range (0.1–1 Hz), the spectral indices of the velocity and magnetic fluctuations are  $-1.51/-1.61$  and  $-1.60/-1.74$  for the first and second intervals, respectively. These values are close to the observations at 1 au where magnetic field spectrum is typically steeper than the velocity (Boldyrev et al. 2011; Chen et al. 2013a; Bowen et al. 2018). The ion-scale spectral break of the magnetic field power spectrum is approximately 5 and 2 Hz in the first and second intervals, respectively, which are at least a factor of six larger than the typical values at 1 au ( $\approx 0.3$  Hz; e.g., Markovskii et al. 2008; Vech et al. 2017). This suggests again that the FA mode is essential to study the  $\delta v$ - $\delta b$  coupling in the kinetic range since velocity fluctuations at these scales are not measured with other operation modes of SPC.

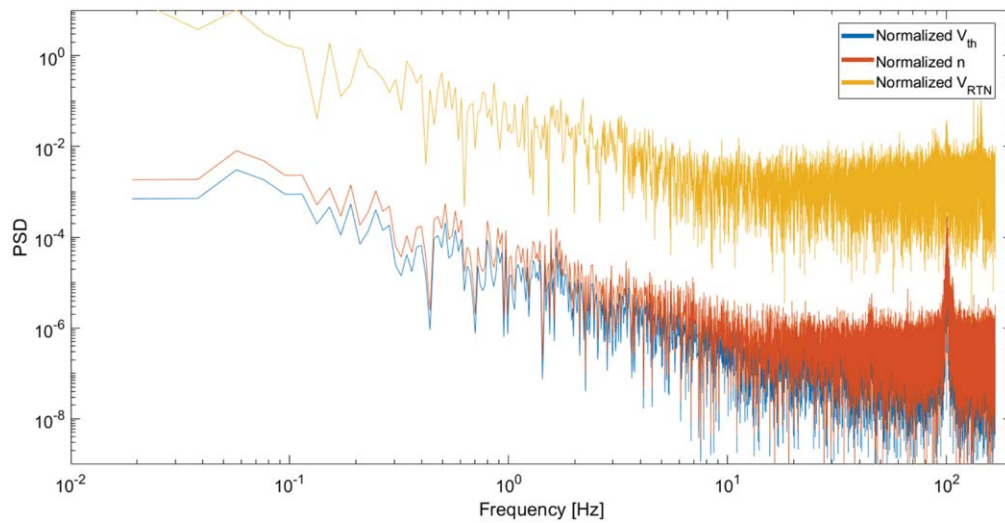
The  $V$ - and  $B$ -field spectral indices show good correlation in the inertial range; at kinetic scales the  $B$ -field spectral index is around  $-2.5$  and  $-3$ , which is similar to the observations at

1 au (e.g., Leamon et al. 1998; Alexandrova et al. 2009), in contrast at kinetic scales we find no signatures of spectral steepening in the  $V$ -field power spectrum. Previous studies found that the power spectrum of ion fluxes show very wide range of features: Riazantseva et al. (2017) categorized power spectra of ion fluxes into five groups using Spektr-R data at 1 au. The most frequently occurring spectra (50% of the cases) showed two slopes and one break point between them at ion-scale, the second most frequent class (32%) showed flattening in the vicinity of the break. In contrast, 6.3% of power spectra did not show steepening at kinetic scales at all. Riazantseva et al. (2017) did not find clear trend (such as  $V_{sw}$  or  $\beta_p$  dependence) in the underlying solar wind parameters that may explain this feature. Based on previous studies (e.g., Chen & Boldyrev 2017), we expect the steepening of the velocity spectra and it is possible that the noise floor of the FA mode data is not low enough to measure such a break scale.

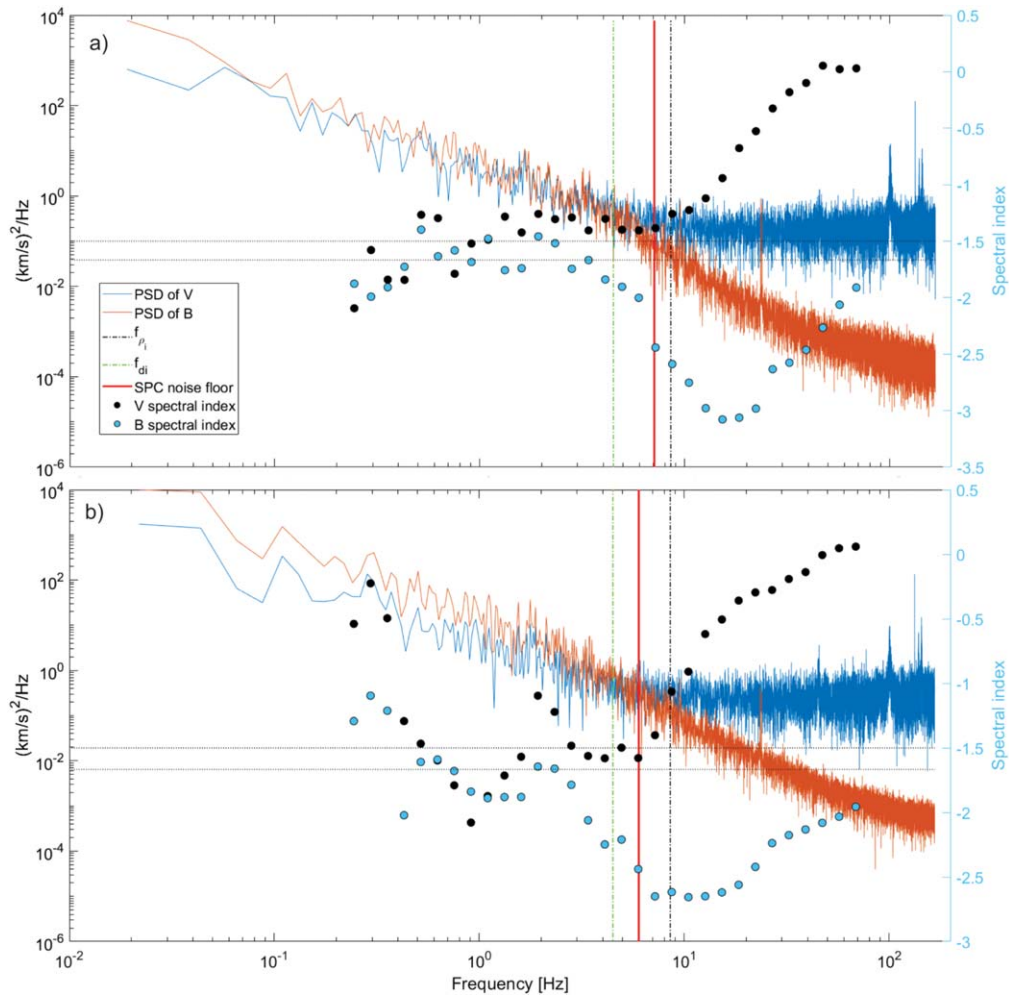
Figure 8 shows the normalized cross helicity, residual energy and cosine of the alignment angle. In Figure 8(a), the normalized cross helicity shows some fluctuations in the inertial range ( $\sigma_c \approx 0.4$ ), which is followed by a sudden decrease near the ion-scale spectral break and convergence to 0 at kinetic scales. In Figure 8(b), the magnetic energy is larger than the energy of velocity fluctuations in the inertial range and  $\sigma_r$  increases gradually toward kinetic scales. Finally, Figure 8(c) suggests that the magnetic and velocity fluctuations are aligned in the inertial range and  $\cos(\theta) = \sigma_c / \sqrt{1 - \sigma_r^2} = 0.5$ ; however, this alignment drops at approximately 1.4 Hz ( $\approx 3.1 d_i$ ), which is comparable to the values found by Parashar et al. (2018) in the solar wind ( $4.4 d_i$ ) at 1 au and in the terrestrial magnetosheath ( $6.5 d_i$ ). Disruption of current sheets with the size of a few  $d_i$  may affect the turbulent cascade and lead to the lack of alignment between  $\delta v$  and  $\delta b$  (see Loureiro & Boldyrev 2017; Mallet et al. 2017; Vech et al. 2018). Another explanation for the loss of alignment is that the turbulence transitions into the kinetic Alfvén range where the



**Figure 5.** Comparison of the trace power spectrum of velocity fluctuations for the 19.6 Hz cadence data when full VDFs were measured and the FA mode data in intervals #1 and #2. For frequencies below 1 Hz, the FA mode data shows remarkably good agreement with the 19.6 Hz data for both intervals.



**Figure 6.** Comparison of the power spectrum of the normalized  $V_{th}$ ,  $n_p$ , and trace velocity fluctuations during the first FA mode interval.



**Figure 7.** Power spectra of velocity and magnetic field fluctuations during the first (a) and second (b) FA mode intervals, respectively.

polarization of the fluctuations changes and the alignment between  $\delta\mathbf{b}$  and  $\delta\mathbf{v}$  ceases to exist (e.g., Schekochihin et al. 2009).

The sudden decrease of the cosine of the alignment angle in Figure 8(c) is close to the flattening of the proton velocity spectra hence we used the following test to quantify the effect of noise. An artificial test velocity data ( $V_{\text{test}}$ ) was computed by adding Gaussian noise to the magnetic field measurements. The amplitude of the noise was empirically chosen such that the trace power spectra of  $V_{\text{test}}$  is in good agreement with the real one in Figure 7. We calculated  $\cos(\theta)$  using  $V_{\text{test}}$  and compared it to the real measurements. We found that in the artificial test data, the alignment drops to zero at a factor of three times a higher frequency than the real measurements; therefore, we suggest that the observed changes of  $\cos(\theta)$  near the break scale are primarily physical and are not caused by Gaussian noise.

#### 4. Conclusion

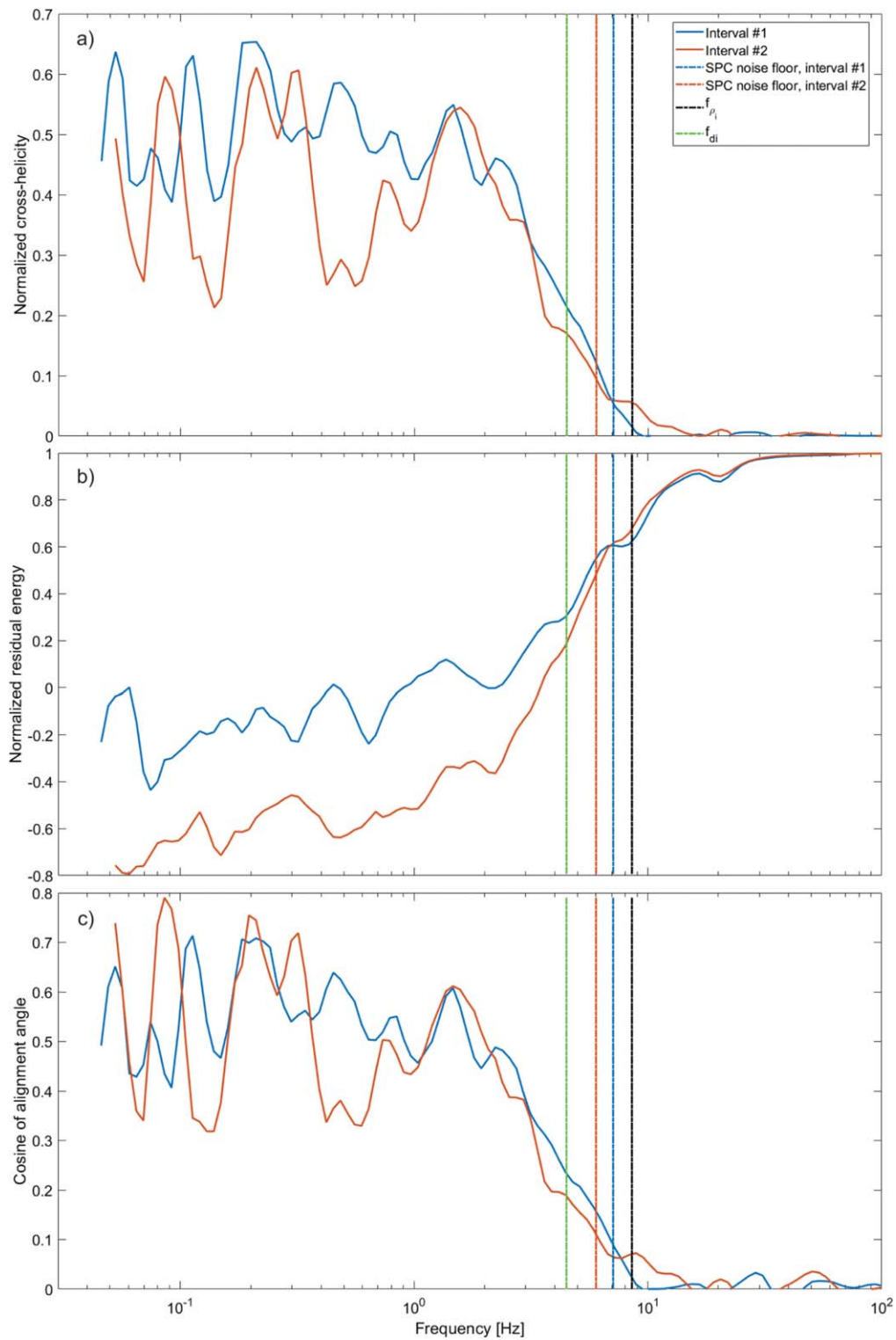
In this work, we presented the first results from the FA operation mode of the Faraday Cup instrument on board the *PSP*. This operation mode allows rapid (up to 293 Hz) measurements of phase space density fluctuations close to the peak of the proton VDF. We described an approach to convert

the measured phase space density fluctuations into vector velocity components, which were found to be reliable up to 7 Hz, which was above the ion-scale spectral break of the magnetic spectrum.

In the inertial range, the velocity and magnetic power spectra were similar to the observations at 1 au; at kinetic scales, the magnetic power spectra steepened (spectral index was  $-2.5/-3$ ), while the velocity power spectra showed no clear break, which is rarely observed at 1 au. The scaling of  $\sigma_c$  and  $\sigma_r$  in the inertial range was similar to larger statistical studies at 1 au (Podesta et al. 2009; Parashar et al. 2018; Verdini et al. 2018). Signatures of alignment between velocity and magnetic fluctuations was found in the inertial range; however, near the ion-scale spectral break (at the scale of  $3.4d_i$ ), we found loss of alignment between velocity and magnetic fluctuations, which might be due to demagnetization of protons.

We expect that with a decreasing perihelion distance, the SPC S/N will improve nearly one order of magnitude and the FA mode will be used several times each day during encounter, allowing us to prepare a statistical study and to investigate proton velocity fluctuations beyond ion-kinetic scales.












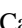



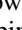


**Figure 8.** Normalized cross helicity, residual energy and cosine of the alignment angle for the first and second FA mode intervals, respectively

The authors are grateful for the reviewer’s constructive comments, which significantly helped to improve the manuscript. The SWEAP Investigation and this publication are supported by the *PSP* mission under NASA contract NNN06AA01C. The *FIELDS* experiment on the *PSP* spacecraft was designed and developed under NASA contract NNN06AA01C. D.V. was supported by NASA’s Future Investigators in NASA Earth and

Space Science and Technology Program Grant 80NSSC19K1430. S.D.B. acknowledges the support of the Leverhulme Trust Visiting Professorship program. Contributions from S.T.B. were supported by NASA Headquarters under the NASA Earth and Space Science Fellowship Program Grant 80NSSC18K1201. K.G.K. was supported by NASA grant NNX16AM23G. J.C.K. was supported by NASA Grant NNX14AR78G. C.H.K.C. is supported by STFC

Ernest Rutherford Fellowship ST/N003748/2. The data used in this study are available from 2019 November 12 at the NASA Space Physics Data Facility (SPDF).

### ORCID iDs

Daniel Vech  <https://orcid.org/0000-0003-1542-1302>  
 Justin C. Kasper  <https://orcid.org/0000-0002-7077-930X>  
 Kristopher G. Klein  <https://orcid.org/0000-0001-6038-1923>  
 Jia Huang  <https://orcid.org/0000-0002-9954-4707>  
 Michael L. Stevens  <https://orcid.org/0000-0002-7728-0085>  
 Christopher H. K. Chen  <https://orcid.org/0000-0003-4529-3620>  
 Anthony W. Case  <https://orcid.org/0000-0002-3520-4041>  
 Kelly Korreck  <https://orcid.org/0000-0001-6095-2490>  
 Stuart D. Bale  <https://orcid.org/0000-0002-1989-3596>  
 Trevor A. Bowen  <https://orcid.org/0000-0002-4625-3332>  
 David Malaspina  <https://orcid.org/0000-0003-1191-1558>  
 Marc Pulupa  <https://orcid.org/0000-0002-1573-7457>  
 Thierry Dudok de Wit  <https://orcid.org/0000-0002-4401-0943>  
 Robert MacDowall  <https://orcid.org/0000-0003-3112-4201>

### References

- Alexandrova, O., Saur, J., Lacombe, C., et al. 2009, *PhRvL*, **103**, 165003  
 Alfvén, H. 1942, *Natur*, **150**, 405  
 Bale, S., Goetz, K., Harvey, P., et al. 2016, *SSRv*, **204**, 49  
 Bale, S., Kellogg, P., Mozer, F., Horbury, T., & Reme, H. 2005, *PhRvL*, **94**, 215002  
 Bale, S. D., Badman, S. T., & Bonnell, J. W. 2019, *Natur*, **576**, 237  
 Boldyrev, S. 2006, *PhRvL*, **96**, 115002  
 Boldyrev, S., Perez, J. C., Borovsky, J. E., & Podesta, J. J. 2011, *ApJL*, **741**, L19  
 Boldyrev, S., Perez, J. C., & Zhdankin, V. 2012, in AIP Conf. Proc. 1436, Physics of the Heliosphere: A 10 Year Retrospective, ed. J. Heerikhuisen et al. (Melville, NY: AIP), 18  
 Bowen, T. A., Mallet, A., Bonnell, J. W., & Bale, S. D. 2018, *ApJ*, **865**, 45  
 Bruno, R., & Bavassano, B. 1991, *JGRA*, **96**, 7841  
 Bruno, R., & Bavassano, B. 1993, *P&SS*, **41**, 677  
 Bruno, R., Bavassano, B., Pietropaolo, E., Carbone, V., & Rosenbauer, H. 1997, *JGRA*, **102**, 14687  
 Case, A. W., Kasper, J. C., Stevens, M. L., et al. 2020, doi:10.3847/1538-4365/ab5a7b  
 Chandran, B. D. 2008, *ApJ*, **685**, 646  
 Chen, C., Bale, S., Salem, C., & Maruca, B. 2013a, *ApJ*, **770**, 125  
 Chen, C., Boldyrev, S., Xia, Q., & Perez, J. 2013b, *PhRvL*, **110**, 225002  
 Chen, C. H., & Boldyrev, S. 2017, *ApJ*, **842**, 122  
 Chen, C. H. K., Bale, S. D., Bonnell, J. W., et al. 2020, doi:10.3847/1538-4365/ab60a3  
 Coleman, P. J., Jr 1968, *ApJ*, **153**, 371  
 Dudok de Wit, T., Krasnoselskikh, V. V., Bale, S. D., et al. 2020, doi:10.3847/1538-4365/ab5853  
 Fox, N., Velli, M., Bale, S., et al. 2016, *SSRv*, **204**, 7  
 Gosling, J., Tian, H., & Phan, T. 2011, *ApJL*, **737**, L35  
 Grappin, R., Mangeney, A., & Marsch, E. 1990, *JGRA*, **95**, 8197  
 Horbury, T., Matteini, L., & Stansby, D. 2018, *MNRAS*, **478**, 1980  
 Huang, J., Kasper, J. C., Vech, D., et al. 2019, arXiv:1912.03871  
 Kasper, J. C., Abiad, R., Austin, G., et al. 2016, *SSRv*, **204**, 131  
 Kasper, J. C., Bale, S. D., & Belcher, J. W. 2019, *Natur*, **576**, 228  
 Leamon, R. J., Smith, C. W., Ness, N. F., Matthaeus, W. H., & Wong, H. K. 1998, *JGRA*, **103**, 4775  
 Loureiro, N. F., & Boldyrev, S. 2017, *ApJ*, **850**, 182  
 Mallet, A., Schekochihin, A. A., & Chandran, B. D. 2017, *JPIPh*, **83**, 905830609  
 Markovskii, S., Vasquez, B. J., & Smith, C. W. 2008, *ApJ*, **675**, 1576  
 Matteini, L., Alexandrova, O., Chen, C., & Lacombe, C. 2016, *MNRAS*, **466**, 945  
 Matthaeus, W., Pouquet, A., Mininni, P. D., Dmitruk, P., & Breech, B. 2008, *PhRvL*, **100**, 085003  
 Matthaeus, W. H., & Goldstein, M. L. 1982, *JGRA*, **87**, 6011  
 McManus, M. D., Bowen, T. A., Mallet, A., et al. 2020, *ApJS*, doi:10.3847/1538-4365/ab6dce  
 Oughton, S., & Matthaeus, W. H. 1995, *JGRA*, **100**, 14783  
 Parashar, T. N., Chasapis, A., Bandyopadhyay, R., et al. 2018, *PhRvL*, **121**, 265101  
 Parashar, T. N., Goldstein, M. L., Maruca, B. A., et al. 2020, doi:10.3847/1538-4365/ab64e6  
 Podesta, J., Roberts, D., & Goldstein, M. 2007, *ApJ*, **664**, 543  
 Podesta, J. J., Chandran, B. D. G., Bhattacharjee, A., Roberts, D. A., & Goldstein, M. L. 2009, *JGRA*, **114**, A01107  
 Riazantseva, M., Budaev, V., Rakhmanova, L., et al. 2017, *JPIPh*, **83**, 705830401  
 Roberts, D., Goldstein, M., Klein, L., & Matthaeus, W. 1987, *JGRA*, **92**, 12023  
 Šafránková, J., Němeček, Z., Němec, F., et al. 2016, *ApJ*, **825**, 121  
 Šafránková, J., Němeček, Z., Přech, L., & Zastenker, G. N. 2013a, *PhRvL*, **110**, 025004  
 Šafránková, J., Němeček, Z., Přech, L., et al. 2013b, *SSRv*, **175**, 165  
 Schekochihin, A., Cowley, S., Dorland, W., et al. 2009, *ApJS*, **182**, 310  
 Smith, C. W., Hamilton, K., Vasquez, B. J., & Leamon, R. J. 2006, *ApJL*, **645**, L85  
 Vech, D., Klein, K. G., & Kasper, J. C. 2017, *ApJL*, **850**, L11  
 Vech, D., Mallet, A., Klein, K. G., & Kasper, J. C. 2018, *ApJL*, **855**, L27  
 Verdini, A., Grappin, R., Alexandrova, O., & Lion, S. 2018, *ApJ*, **853**, 85  
 Wang, Y., Boldyrev, S., & Perez, J. C. 2011, *ApJL*, **740**, L36  
 Wicks, R. T., Roberts, D. A., Mallet, A., et al. 2013, *ApJ*, **778**, 177